

ACCELERATION PHASES OF A SOLAR FILAMENT DURING ITS ERUPTION

H.Q. SONG¹, Y. CHEN¹, J. ZHANG², X. CHENG³, H. Fu¹, AND G. LI⁴

1 Shandong Provincial Key Laboratory of Optical Astronomy and Solar-Terrestrial Environment, and Institute of Space Sciences, Shandong University, Weihai, Shandong 264209, China

`hqsong@sdu.edu.cn`

2 School of Physics, Astronomy and Computational Sciences, George Mason University, Fairfax, VA 22030, USA

3 School of Astronomy and Space Science, Nanjing University, Nanjing, Jiangsu 210093, China

4 Department of Space Science and CSPAR, University of Alabama in Huntsville, Huntsville, AL 35899, USA

ABSTRACT

Filament eruptions often lead to coronal mass ejections (CMEs), which can affect critical technological systems in space and on the ground when they interact with the geo-magnetosphere in high speeds. Therefore, it is an important issue to investigate the acceleration mechanisms of CMEs in solar/space physics. Based on observations and simulations, the resistive magnetic reconnection and the ideal instability of magnetic flux rope have been proposed to accelerate CMEs. **However, it remains elusive whether both of them play a comparable role during a particular eruption.** It has been extremely difficult to separate their contributions as they often work in a close time sequence during one fast acceleration phase. Here we report an intriguing filament eruption event, which shows two apparently separated fast acceleration phases and provides us an excellent opportunity to address the issue. Through analyzing the correlations between velocity (acceleration) and soft (hard) X-ray profiles, we suggest that the instability and magnetic reconnection make a major contribution during the first and second fast acceleration phases, respectively. Further, we find that both processes have a comparable contribution to accelerate the filament in this event.

Subject headings: magnetic reconnection – Sun: flares – Sun: coronal mass ejections (CMEs)

1. INTRODUCTION

Coronal mass ejections (CMEs) are the most energetic eruptions in the solar system and can affect critical technological systems in space and on the ground when they interact with the geo-magnetosphere in high speeds ranging from several hundred to even more than one thousand kilometers per second. Therefore, it is an important issue to investigate the acceleration mechanisms of CMEs in solar/space physics. It is generally accepted that CMEs are driven by magnetic flux rope (MFR) eruptions (Chen 2011). However, we can not observe MFR structures directly in the corona because no instrument can provide the high quality measurement of the coronal magnetic field at present. Several lines of observations in the lower corona have been proposed as the proxies of MFRs, e.g., filaments/prominences (Rust & Kumar 1994), coronal cavities (Wang & Stenborg 2010), sigmoids (Titov & Démoulin 1999; McKenzie & Canfield 2008), and hot channels (Zhang et al. 2012; Song et al. 2014a, 2014b, 2015). Resolving the dynamics of these structures are critical to our understanding of the CME acceleration process.

There exist two important magnetic energy release mechanisms: one is the resistive magnetic reconnection process (Carmichael 1964; Sturrock 1966; Hirayama 1974; Kopp & Pneuman 1976) and the other is the ideal global magnetohydrodynamic (MHD) MFR instability (van Tend & Kuperus 1978; Priest & Forbes 1990; Forbes & Isenberg 1991; Isenberg et al. 1993; Forbes & Priest 1995; Hu et al. 2003; Kliem & Török 2006; Fan & Gibson 2007; Chen et al. 2007a, 2007b; Olmedo & Zhang 2010). Both mechanisms are supported by observations. For example, good correlations exist between CME speed (acceleration) and the soft X-ray (hard X-ray and microwave) profiles of associated flares (Zhang et al. 2001; Qiu et al. 2004; Maričić et al. 2007). In addition, studies showed that the extrapolated magnetic flux in the flaring region was comparable with the magnetic flux of the MFR reconstructed from in situ data (Qiu et al. 2007). All these CME-flare association studies support that reconnections play an important role in accelerating CMEs. On the other hand, statistical studies showed that the projected speed in the sky plane and kinetic energy of CMEs only had weak correlations with the peak values of their associated X-ray flares (Yashiro et al. 2002; Vršnak et al. 2005). These observations support that the ideal MHD instability also makes significant contributions to the CME acceleration besides the magnetic reconnection.

The theoretical and simulation studies also support that the instability and reconnection can accelerate the CMEs (Démoulin & Aulanier 2010; Roussev et al. 2012; Amari et al. 2014). Generally, the instability plays an important role in triggering and accelerating the MFR, and then the magnetic reconnection accelerates the MFR further and allows the process to develop continuously (Priest & Forbes 2002; Lin et al. 2003).

However, it remains elusive whether both mechanisms have a comparable contri-

bution to the acceleration in a particular event as they usually accelerate CMEs in a close time sequence. In this letter, we address this issue through analyzing a filament eruption with two apparently separated fast acceleration phases, instead of one as usual. The relevant observations and results are described in Section 2. Section 3 presents the related discussion, which is followed by a summary in Section 4.

2. OBSERVATIONS AND RESULTS

2.1. Instruments

The eruption process was recorded by the Atmospheric Imaging Assembly (AIA) telescope (Lemen et al. 2012) on board the *Solar Dynamic Observatory (SDO)*. AIA has 10 narrow UV and EUV passbands with a cadence of 12 s, a spatial resolution of $1.2''$, and an FOV of $1.3 R_{\odot}$. The AIA images shown in this letter (Figure 1 and Supplementary Movie) are a small portion of the original full size images.

The soft and hard X-ray (SXR and HXR) data shown in Figure 3 are from *Geostationary Operational Environment Satellite (GOES)* and the *Reuven Ramaty High Energy Solar Spectroscopic Imager (RHESSI; Lin et al. 2002)*, respectively. *GOES* provides the integrated full-disk SXR emission from the Sun, which are used to characterize the magnitude, onset time, and peak time of solar flares. *RHESSI* provides the HXR spectrum and imaging of solar flares.

2.2. Overview of the filament eruption

The filament eruption originated from NOAA Active Region 12151 located at the heliographic coordinates \sim S09E76 on 2014 August 24. This eruption produced an M5.9 class SXR flare on *GOES* scale, which started at 12:00 UT and peaked at 12:17 UT. A CME (linear velocity 417 km s^{-1}) associated with it was recorded by the Large Angle Spectroscopic Coronagraph (LASCO, Brueckner et al. 1995) on board the *Solar Heliospheric Observatory*. We inspect the AIA images and find that the filament appeared in all bandpasses corresponding to the coronal and chromospheric temperatures, which indicate that it has a multi-thermal nature. The eruption process snapshots observed with 304 \AA ($\sim 0.05 \text{ MK}$), 171 \AA ($\sim 0.6 \text{ MK}$) and 335 \AA ($\sim 2.5 \text{ MK}$) are presented at the top, middle and bottom panels of Figure 1, respectively. The time when the image was taken is shown at the top of each panel. The arrows depict the EUV brightening positions, where the plasma was heated by magnetic reconnection. The full AIA image sequences of the eruption in six passbands are provided in the Supplementary Movie.

In order to clearly display the rising motion of the filament, a slice-time plot was constructed with base-difference images of 304 \AA along the dotted line in panel b of Figure 1, as presented in Figure 2. Around 12:16:00 UT, the filament apex moved out of the field of view (FOV) of AIA,

so no further kinematic evolution analysis was possible after that time. Through the time-stacking plot, we measure the filament height with time for a careful kinematic analysis as described in next subsection.

2.3. Acceleration processes of the filament

The kinematic information of the filament is obtained by analyzing AIA 304 Å base-difference images. We carefully inspect the images and identify the filament leading edges along the slice in Figure 1(b). The heights are measured from the projected distance of the leading edges from the flare location. The uncertainty of the height measurement is about 4 pixels (2 Mm), which are propagated to estimate the velocity errors in the standard way. Based on the height-time measurements, the velocities are derived from a numerical derivative method that employs Lagrangian interpolation of three neighboring points, a piecewise approach to calculate the velocity (Zhang et al. 2001; Cheng et al. 2013; Song et al. 2014a, 2014b). Then the filament acceleration is calculated with the same method based on the calculated velocity profile.

Figure 3 presents the kinematic analysis results. The entire eruption process as seen by AIA can be divided into three distinct phases as shown in panel a: an initial slow-rise phase, and then two fast acceleration phases. The vertical green solid lines on the left and right demarcate the start time of the first and second fast acceleration phases, respectively. In addition, the SXR flux with time can also be divided into a slow-rise phase and two impulsive phases. The vertical black dotted line denotes the onset of the first impulsive phase of X-ray flare. Apparently, the right green solid line also marks the onset of the second impulsive phase of the flare.

The slow-rise phase of the filament lasted for about 7 min from $\sim 12:00$ to $\sim 12:07$ UT; at the end of this phase, the velocity increased to ~ 40 km s $^{-1}$ with an averaged acceleration of 95 m s $^{-2}$. The first fast acceleration phase started around 12:07:19 UT and ended around 12:11:31 UT when the velocity reached to ~ 450 km s $^{-1}$ with an averaged acceleration of ~ 1626 m s $^{-2}$. Then the velocity decreased slightly during the following ~ 1.5 minutes. The second fast acceleration phase started around 12:13:00 UT. As the filament moved out of the AIA FOV, we can trace a part of the second acceleration phase. The final velocity we deduce is ~ 700 km s $^{-1}$ around 12:15:40 UT. Therefore, the averaged acceleration for this phase is ~ 1600 m s $^{-2}$. The horizontal red solid lines in Figure 3 depict these two fast acceleration periods. As mentioned, the SXR flux with time has two impulsive phases, which indicate there exist two obvious reconnection processes. This point is further confirmed by the derivation of the SXR flux with two peaks as shown in panel b. The two red dots in panels b and c depict the positions of two peaks, which show that the first obvious reconnection is weak compared with the second one.

The onset of CME acceleration phase often coincides well with the onset of accompanying flares (Zhang et al. 2001). For our event, it is obvious that the velocity and SXR flux profiles are tightly consistent during their slow-rise phase and second fast acceleration phase. However,

the onset time of the first fast acceleration phase of filament (12:07:19 UT) is obviously ahead of the first impulsive phase of flare (12:09:19 UT) for two minutes, which means the filament was accelerated before the first obvious reconnection onset. Thanks to AIA’s high cadence, such short difference is otherwise difficult to observe and measure.

Further, we plot the HXR flux versus time in panel c, along with the filament acceleration profile. The error bars of acceleration are large and not shown here. Note the HXR rates fell after 12:05 UT when the thin attenuators moved into the detector FOV, and it fell suddenly again before 12:18 UT when *RHESSI* went into night. We made two Gaussian fitting for the HXR flux as presented with two thin blue solid curves in the panel. We believe the two fitted Gaussian shapes correspond to the two obvious reconnection processes according to the derivation of SXR flux in panel b. The observed HXR peaks in the middle of the two fitted peaks should be due to the overlapping effect of HXR emission from these two reconnections, which is supported by the accumulation of the two fitted curves as shown with the thick blue solid curve. Panel c shows that the first fast acceleration profile did not have any correlations with the HXR flux, even the acceleration continued to decrease after the reconnection onset. They tightly correlated with each other only during the second fast acceleration process. **Therefore, we suggest that the first fast acceleration process was induced by the instability (Cheng et al. 2013), while the second one was accelerated mainly through the subsequent magnetic reconnection (Priest & Forbes 2002; Lin et al. 2003).** The AIA 335 Å observations present a kink morphology during the eruption (See Figure 1(h)), indicating that the filament might be accelerated through the MFR kink instability (Cheng et al. 2014). Our study suggests that both mechanisms have a comparable contribution to the CME acceleration, which is consistent with the MHD simulation results (Chen et al. 2007b).

3. DISCUSSION

Our observational results have significant theoretical implications. **The event provides us an excellent opportunity to compare the contributions of different acceleration mechanisms.** During the eruption, the filament first exhibits a slow-rise phase, followed by two fast acceleration phases. For the slow-rise phase, the acceleration might be induced by the initial weak quasi-separatrix-layer (QSL) reconnection (Cheng et al. 2013), i.e., reconnections at the interface between filament and its surrounding corona. The brightening as shown with arrows in Figures 1(a) and (d) indicated that there existed reconnection during that period (Cheng et al. 2013). Another possibility is that the slow-rise phase was due to the initial acceleration stage caused by the MFR kink instability. It is not possible to distinguish their contributions at this phase.

However, for the following two fast acceleration phases, we suggest that they are attributed to the instability and the reconnection, respectively. It can be seen that the first obvious reconnection didn’t result in any considerable filament acceleration. This might be explained by two possible factors: first, the reconnection is weaker compared to the second one according to their HXR peak values as mentioned above. **This weak reconnection might be insufficient to accelerate**

the MFR as it can not weaken the tension force of the overlying magnetic loops fast enough, and may even lead to the MFR deceleration as calculated by Lin & Forbes (2000) and Lin (2002); second, it is likely that this reconnection is still the QSL reconnection, as told from the HXR data of *RHESSI*. The locations of the HXR sources are shown as black contours at 70%, 80%, and 90% of the maximum in the 25-50 keV band (Figures 1(b),(c),(e),(f)). The sources are mainly at the two footpoints of the filament during the first obvious reconnection (Figures 1(b),(e)), which is consistent with the QSL reconnection. The QSL reconnection can heat the filament (as depicted with arrows in Figures 1(b) and (e)) (Cheng et al. 2013) and produce high energy electrons that escape along two legs of the filament and produce HXR emission at the footpoints, but it does not contribute to accelerate filament. On the other hand, the HXR sources locate mainly between the two footpoints during the second obvious reconnection (Figures 1(c),(f)), which indicates the reconnection mainly took place in the current sheet connecting the filament to the flare loop. This reconnection can accelerate filament/MFR (Carmichael 1964; Sturrock 1966; Hirayama 1974; Kopp & Pneuman 1976; Lin & Forbes 2000; Lin 2002; Chen 2011) and produce energetic electrons that hit the flare loop to produce the *RHESSI* HXR source.

If there was not the first obvious magnetic reconnection, and the second obvious reconnection took place quickly after the kink instability onset, we will not be able to distinguish the contributions from the instability and reconnection, and we should observe only one fast acceleration phase like most events. Therefore, we point out that the time difference between the instability onset and the subsequent reconnection in the current sheet should be long enough to distinguish their contributions. We conjecture that this time difference is very short in most events, which might be one important reason that similar events with two fast acceleration phases are rare.

4. SUMMARY

A filament eruption associated with an M5.9 class flare was well observed by the AIA at the southeast limb of the Sun on 2014 August 24, which presented two fast acceleration phases during the eruption and provided us a perfect opportunity to compare the contributions of different acceleration mechanisms of CMEs/MFRs during a particular event. Based on the detailed analysis of the relations between velocity (acceleration) and SXR (HXR) profiles, we suggest that the instability and magnetic reconnection make a major contribution during the first and second fast acceleration phases, respectively. The averaged acceleration for the first phase is $\sim 1626 \text{ m s}^{-2}$, similar to that of the second phase ($\sim 1600 \text{ m s}^{-2}$). Therefore, both instability and reconnection play a comparable role to accelerate the filament in this event, which is consistent with the MHD simulation results (Chen et al. 2007b). We summarize the two fast acceleration phases as follow: the instability takes place first in a catastrophic manner, then the MFR is accelerated by the Lorentz force (Chen et al. 2007b; Amari et al. 2014). The magnetic energy is mainly transformed into the kinetic energy of MFR. In the meanwhile, current sheet is bound to form as the eruptive MFR drags magnetic field lines outwards,

which provides proper site for fast magnetic reconnection. The subsequent reconnection produces a further acceleration of the MFR, i.e., the second fast acceleration phase.

We thank the referee for his/her valuable comments that improved the manuscript. SDO is a mission of NASA's Living With a Star Program. This work is supported by the 973 program 2012CB825601, NNSFC grants 41274177, 41274175, and 41331068. J.Z. is supported by US NSF AGS-1249270 and NSF AGS-1156120.

REFERENCES

- Amari, T., Canou, A., & Aly, J.-J. 2014, *Nature*, 514, 465
- Brueckner, G. E., Howard, R. A., Koomen, M. J., et al. 1995, *Sol. Phys.*, 162, 357
- Carmichael, H. 1964, *NASA Special Publication*, 50, 451
- Chen, P. F. 2011, *Living Reviews in Solar Physics*, 8, 1
- Chen, Y., Hu, Y. Q., & Sun, S. J. 2007a, *ApJ*, 665, 1421
- Chen, Y., Hu, Y. Q., & Xia, L. D. 2007b, *Advances in Space Research*, 40, 1780
- Cheng, X., Ding, M. D., Zhang, J., et al. 2014, *ApJ*, 789, L35
- Cheng, X., Zhang, J., Ding, M. D., et al. 2013, *ApJ*, 769, L25
- Démoulin, P., & Aulanier, G. 2010, *ApJ*, 718, 1388
- Fan, Y., & Gibson, S. E. 2007, *ApJ*, 668, 1232
- Forbes, T. G., & Isenberg, P. A. 1991, *ApJ*, 373, 294
- Forbes, T. G., & Priest, E. R. 1995, *ApJ*, 446, 377
- Hirayama, T. 1974, *Sol. Phys.*, 34, 323
- Hu, Y. Q., Li, G. Q., & Xing, X. Y. 2003, *Journal of Geophysical Research (Space Physics)*, 108, 1072
- Isenberg, P. A., Forbes, T. G., & Demoulin, P. 1993, *ApJ*, 417, 368
- Kliem, B., & Török, T. 2006, *Physical Review Letters*, 96, 255002
- Kopp, R. A., & Pneuman, G. W. 1976, *Sol. Phys.*, 50, 85
- Lemen, J. R., Title, A. M., Akin, D. J., et al. 2012, *Sol. Phys.*, 275, 17

- Lin J. 2002, *Chin. J. Astron. Astrophys.*, 2, 539
- Lin J., & Forbes, T. G. 2000, *J. Geophys. Res.*, 105, 2375
- Lin, J., Soon, W., Baliunas, S. L. 2003, *New Astronomy Reviews*, 47, 53
- Lin, R. P., Dennis, B. R., Hurford, G. J., et al. 2002, *Sol. Phys.*, 210, 3
- Maričić, D., Vršnak, B., Stanger, A. L., et al. 2007, *Sol. Phys.*, 241, 99
- McKenzie, D. E., & Canfield, R. C. 2008, *A&A*, 481, L65
- Olmedo, O., & Zhang, J. 2010, *ApJ*, 718, 433
- Priest, E. R., & Forbes, T. G. 1990, *Sol. Phys.*, 126, 319
- Priest, E. R., & Forbes, T. G. 2000, *The Astronomy and Astrophysics Review*, 10, 313
- Qiu, J., Hu, Q., Howard, T. A., & Yurchyshyn, V. B. 2007, *ApJ*, 659, 758
- Qiu, J., Wang, H., Cheng, C. Z., & Gary, D. E. 2004, *ApJ*, 604, 900
- Roussev, I. I., Galsgaard, K., Downs, C., et al. 2012, *Nature Physics*, 8, 845
- Rust, D. M., & Kumar, A. 1994, *Sol. Phys.*, 155, 69
- Song, H. Q., Chen, Y., Zhang, J., et al. 2015, *ApJ*, in press
- Song, H. Q., Zhang, J., Chen, Y., & Cheng, X. 2014a, *ApJ*, 792, L40
- Song, H. Q., Zhang, J., Cheng, X., et al. 2014b, *ApJ*, 784, 48
- Sturrock, P. A. 1966, *Natur*, 211, 695
- Titov, V. S., & Démoulin, P. 1999, *A&A*, 351, 707
- van Tend, W., & Kuperus, M. 1978, *Sol. Phys.*, 59, 115
- Vršnak, B., Sudar, D., & Ruždjak, D. 2005, *A&A*, 435, 1149
- Wang, Y.-M., & Stenborg, G. 2010, *ApJ*, 719, L181
- Yashiro, S., Gopalswamy, N., Michalek, G., & Howard, R. A. 2002, *BAAS*, 34, 695
- Zhang, J., Dere, K. P., Howard, R. A., Kundu, M. R., & White, S. M. 2001, *ApJ*, 559, 452
- Zhang, J., Cheng, X., & Ding, M.-D. 2012, *Nature Communications*, 3, 747

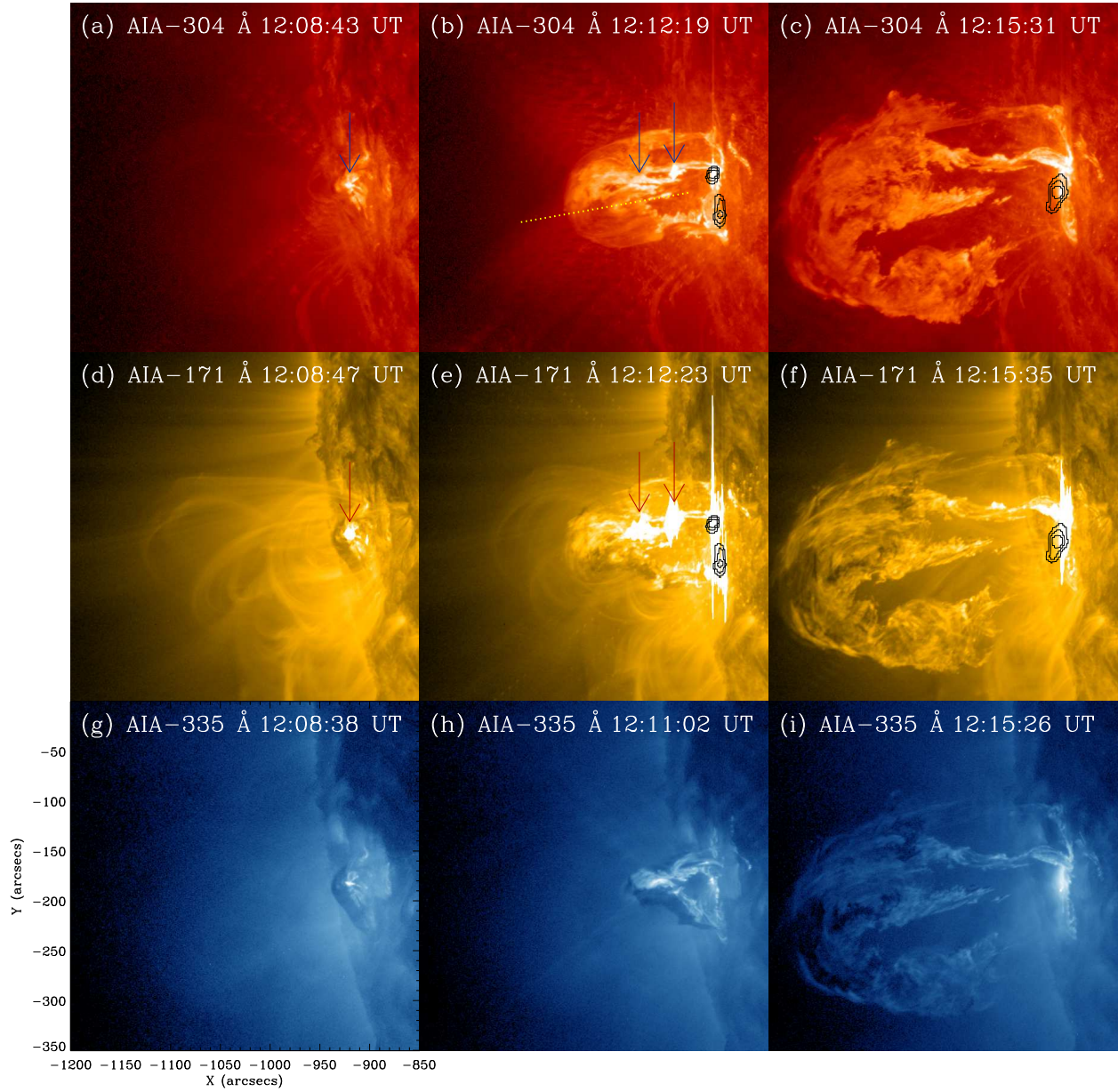


Fig. 1.— Filament eruption event on 2014 August 24 observed in AIA images. (A color version and animation of this figure are available in the online journal.)

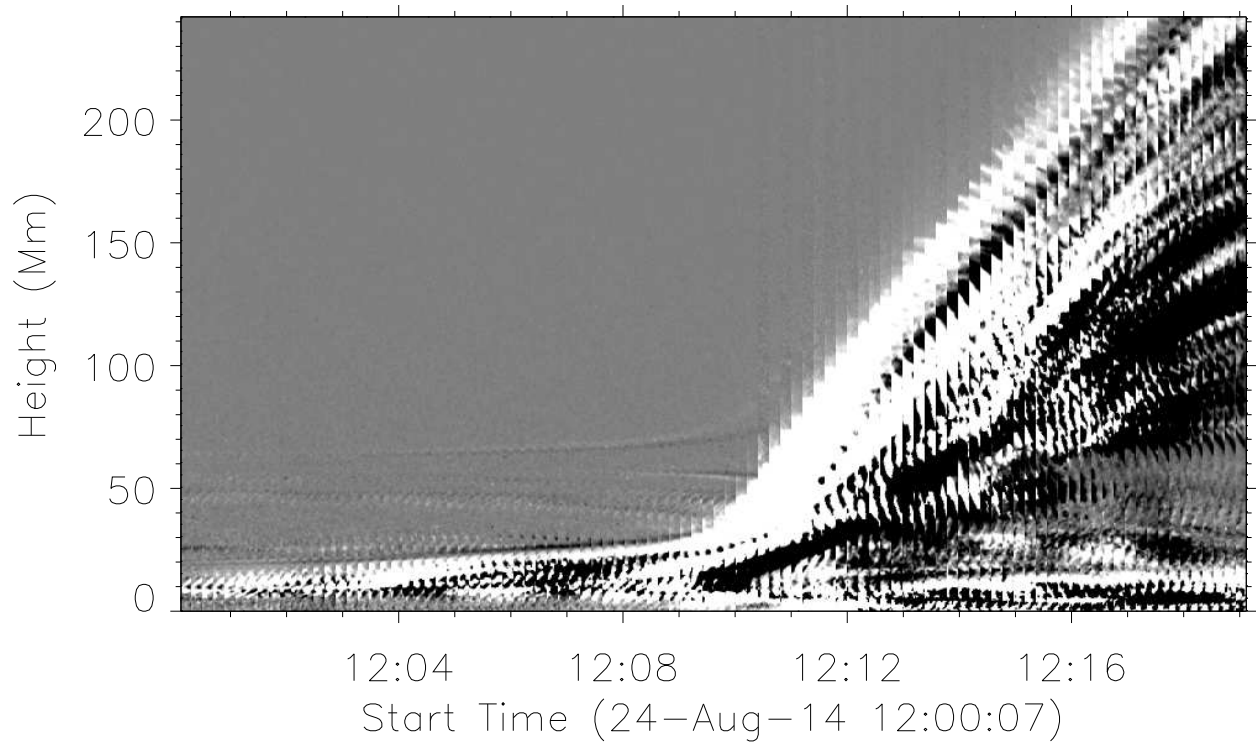


Fig. 2.— The constructed slice-time plots illustrating the rising motion of the filament.

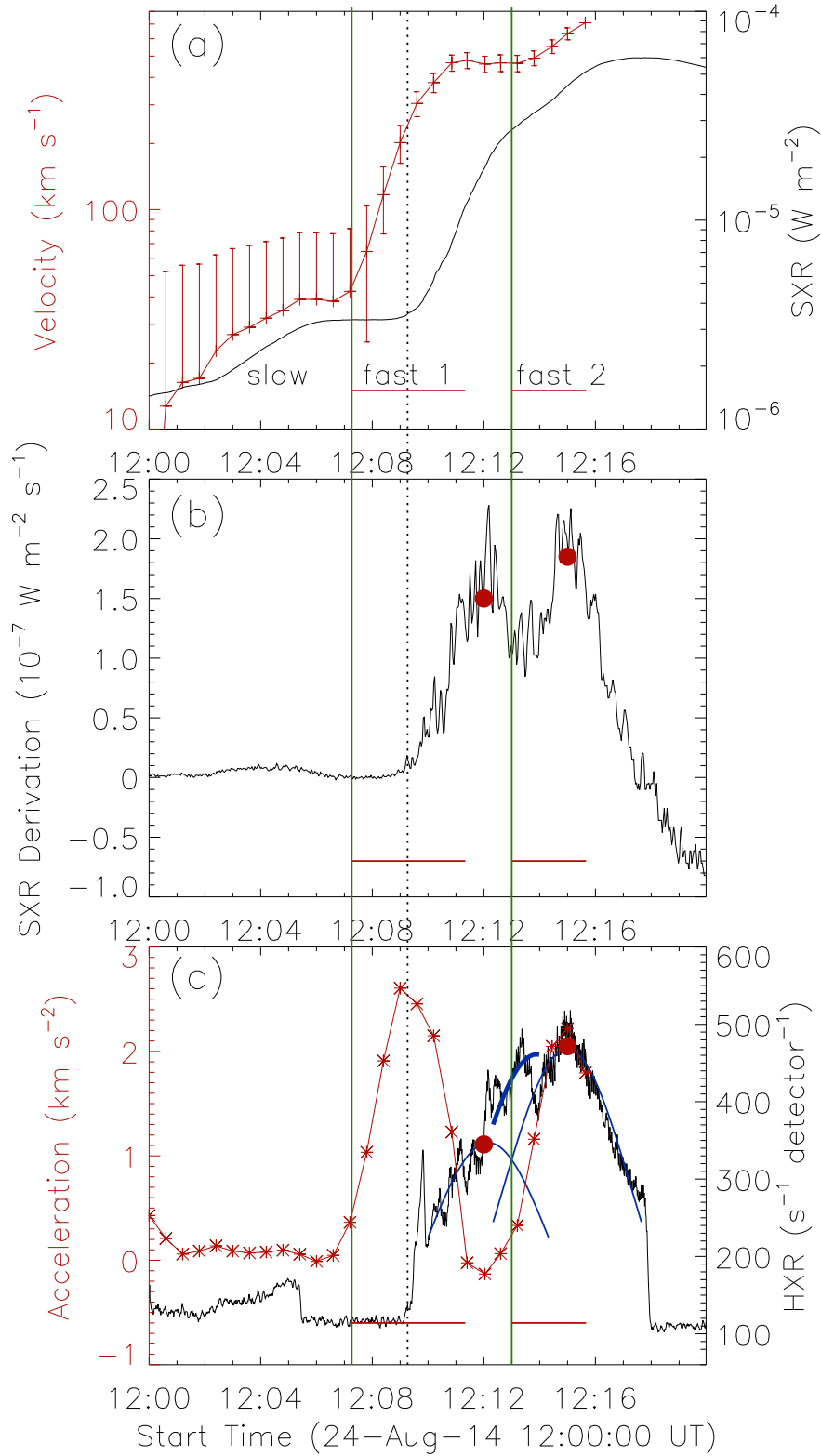


Fig. 3.— (a) The velocity-time plots of the filament (red solid line), along with *GOES* SXR 1–8 Å flux profiles of the accompanying flare. (b) The derivation of the SXR flux. (c) The acceleration-time plots (red solid curve), along with *RHESSI* HXR 12–25 keV (black solid curve) and their gaussian fittings (blue solid curve). (A color version of this figure is available in the online journal.)